Applied and Environmental Microbiology, Feb. 2011, p. 1254–1262 Vol. 77, No. 4
0099-2240/11/$12.00 doi:10.1128/AEM.02001-10

Imaging Hydrated Microbial Extracellular Polymers: Comparative Analysis by Electron Microscopy▽†

Alice C. Dohnalkova,[1]* Matthew J. Marshall,[2] Bruce W. Arey,[1] Kenneth H. Williams,[3] Edgar C. Buck,[4] and James K. Fredrickson[2]

Environmental Molecular Sciences Laboratory, Pacific Northwest National Laboratory, 902 Battelle Boulevard, Richland, Washington 99354[1]; Environmental Microbiology, Fundamental & Computational Sciences Division, Pacific Northwest National Laboratory, 3330 Stevens Drive, Richland, Washington 99354[2]; Earth Sciences Division, Lawrence Berkeley National Laboratory, 1 Cyclotron Road, Berkeley, California 94720[3]; and Energy and Environment Directorate, Pacific Northwest National Laboratory, 325 Redwood St., Richland, Washington 99354[4]

Received 24 August 2010/Accepted 4 December 2010

Microbe-mineral and -metal interactions represent a major intersection between the biosphere and geosphere but require high-resolution imaging and analytical tools for investigation of microscale associations. Electron microscopy has been used extensively for geomicrobial investigations, and although used *bona fide*, the traditional methods of sample preparation do not preserve the native morphology of microbiological components, especially extracellular polymers. Herein, we present a direct comparative analysis of microbial interactions by conventional electron microscopy approaches with imaging at room temperature and a suite of cryogenic electron microscopy methods providing imaging in the close-to-natural hydrated state. *In situ*, we observed an irreversible transformation of the hydrated bacterial extracellular polymers during the traditional dehydration-based sample preparation that resulted in their collapse into filamentous structures. Dehydration-induced polymer collapse can lead to inaccurate spatial relationships and hence could subsequently affect conclusions regarding the nature of interactions between microbial extracellular polymers and their environment.

Electron microscopy (EM)-based imaging and analyses provide excellent high-resolution tools for studying the structural and compositional features of microorganisms and their immediate surroundings. However, the conventional sample processing that includes dehydration as a prerequisite for imaging by high-resolution vacuum instruments can cause substantial changes in microbial cell ultrastructure. Chemical fixation with aldehydes and treatment with heavy metals help to preserve cell morphology and enhance contrast but can also result in substantial shrinkage (41). Dehydration with organic solvents can extract cell constituents, cause cell membrane discontinuities (23), induce distortion of delicate structures such as membrane-associated components (4), and have other deleterious effects on morphology that can consequently lead to inaccurate interpretations of cellular features.

To reduce the damage inherent in these treatments, various innovative cryogenic sample preparation methods have been developed (14, 50). Introduction of the high-pressure freezing coupled with freeze-substitution process brought revolutionary improvements to the EM-based imaging of bacterial cells and associated extracellular material, allowing visualization of such subcellular structures as ribosomes and membrane components (25, 26, 60). In particular, cryo-electron microscopy (cryo-EM) enabled imaging of biological materials in the nearly fully hydrated, closest-to-natural state (39). Based on preventing ice crystal growth by inducing rapid transformation of cellular water to amorphous ice (vitrification) during the sample preparation and imaging at subzero (°C) temperatures to lower the water vapor pressure under an EM vacuum, cryo-EM provided an exceptional technique for analysis of complex biological ultrastructures and macromolecular organization (20, 47). Devoid of the influences of chemical fixatives, dehydration, or heavy metal staining, cryo-EM can provide morphologically accurate images of rapidly frozen living cells and various complexes (7, 54, 62). In fact, when thawed, the vitrified bacteria could regain more than 70% of viability (12).

Bacterially secreted extracellular polymeric substances (EPS), forming the matrix of microbial biofilms, present a remarkable dynamic material that plays critical functional roles in many important processes, such as dental plaque formation, anaerobic corrosion of metals, attachment of pathogens to host cells, and a wide variety of geomicrobial processes in soil, sediment, rock, and marine environments (9, 61). EPS is primarily associated with physical adhesiveness, which plays a major role in bacterial flocculation, biofilm formation, cell adhesion to solid surfaces, and creation of protective microhabitats against adverse environmental conditions, including desiccation, assault by antimicrobial agents, and oxidative stress (30, 40, 43). Additionally, due to its immense absorptive capacity, EPS is capable of binding, accumulating, and sequestering dissolved organic matter and metals from the environ-

* Corresponding author. Mailing address: 902 Battelle Blvd., P.O. Box 999, MSIN K8-93, Richland, WA 99354. Phone: (509) 371-6515. Fax: (509) 371-7866. E-mail: Alice.dohnalkova@pnl.gov.

† Supplemental material for this article may be found at http://aem.asm.org/.

▽ Published ahead of print on 17 December 2010.

ment and is consequently able to influence a wide range of biogeochemical processes. These processes include the dissolution and precipitation of minerals and the transformation of metals and radionuclides, including redox and/or complexation reactions (10, 46).

Generally composed of bacterially secreted heterogeneous combinations of high-molecular-weight polysaccharides, lipids, phosphate, proteins, and nucleic acids, as well as variable amounts of structural components such as flagella, pili, membrane vesicles, and cellular debris, EPS mass can consist of up to 95% of bound and unbound water (16, 53, 61). Due to this extreme hydration, EPS is among the most difficult biological structures to preserve and characterize in its native state and presents a major challenge for obtaining accurate high-resolution images via electron microscopy.

Bacterial EPS has been described as "collapsing into the thick bundles" upon the exposure to traditional organic solvents during dehydration (2). Comparative reports on EPS visualization by EM (28, 52, 55) and studies focused on improving EPS morphology by incubation with multivalent cationic dyes, heavy metals, or gold-conjugated lectins (13, 14, 34) greatly improved the morphological characterization of EPS. Unfortunately, these efforts still employed complete or partial dehydration steps, which prohibited the visualization of EPS in its nearest-to-native, hydrated state. To obtain precise structural information, approaches are needed that preserve the morphology of all bacterial components, especially extracellular material.

The scientific interest in microbial metal and mineral interaction requires obtaining reliable information on the physical association of bacteria, EPS, and metals and/or mineral phases in the natural hydrated state. The selection of the cryo-EM methods proved to be an effective tool for these investigations. The scheme of stabilizing the microbial material with vitreous ice, hence preventing its collapse in a vacuum during EM imaging, allowed the acquisition of accurate cellular morphological information that can be used for modeling bacterial processes; this also allowed documentation of unprecedented views of newly formed biominerals associated with the EPS. In addition, complementary EM techniques were used to directly observe the dynamic process of water loss during dehydration and to correlate these observations with fully hydrated cells and their surrounding EPS to obtain a more complete view of EPS collapse induced by water removal. Consequently, an analysis of the collected image data was provided in accordance with the concept of plastic deformation of viscoelastic material under stress conditions.

MATERIALS AND METHODS

Cells and media. (i) Cell suspensions. Suspensions of washed, resting cells of *Shewanella oneidensis* strain MR-1 (ATCC 700550^T) with a final density of 2×10^8 cells/ml were prepared as previously described (36). The reduction assays were conducted in 30 mM sodium bicarbonate buffer (pH 7.0) with 10 mM sodium lactate as the sole electron donor and a final concentration of either (i) 250 μM U(VI) as uranyl acetate, (ii) 1.0 mM Mn(IV) as the laboratory-synthesized mineral vernadite (31), or (iii) 1.0 mM sodium fumarate as the sole electron acceptors. The assay tubes were purged with an N_2-CO_2 gas mixture (80:20 [vol/vol]) and sealed prior to the addition of cells, followed by horizontal incubation at 30°C with slow gyratory shaking (25 rpm). The reduction of U(VI) or Mn(IV) was determined as previously described (36, 37, 49).

(ii) Biofilms. Natural biofilms of sulfate-reducing bacterial consortia were obtained from a borehole used for long-term (110-day) acetate injection during biostimulation activities at the Department of Energy's (DOE's) Integrated Field Research Challenge site near Rifle, CO (http://ifcrifle.pnl.gov/). Small biofilm samples were removed from the exterior surface of tubing located within an injection borehole after 90 days of acetate addition. Samples were scraped from the tubing surface with a sterile razor blade, and the mineral-encrusted biofilms were immediately immersed and sealed in groundwater pumped from the sampling borehole before being shipped overnight at 4°C to the microscopy facility.

Cryo-TEM preparation. The Vitrobot freeze-plunging apparatus (Mark III; FEI, Hillsboro, OR) was used for the cryo-immobilization of bacterial suspensions. Five microliters of planktonic *Shewanella* cell suspensions was applied on freshly glow-discharged Quantifoil R 2/2 grids (Electron Microscopy Sciences [EMS], Hatfield, PA). The cells were allowed to adhere to the grids for 30 s before being blotted twice (1 s each, offset of −1) on discs of filter paper placed in a Vitrobot humidified chamber to remove excess water. Cells in the remaining very thin aqueous layer were immediately plunge frozen by immersion into a reservoir with liquid ethane cooled by liquid nitrogen within the Vitrobot instrument. The grids with frozen bacterial suspensions were transferred under liquid nitrogen to the Gatan 626 cryo-transmission EM (cryo-TEM) holder (Gatan, Inc., Pleasanton, CA), using the cryo-transfer station (Gatan). After inserting the cryo-holder to the transmission electron microscope, the temperature was maintained below −178°C at all times during the cryo-imaging unless otherwise noted.

Correlated cryo-TEM and RT TEM. During the cryo-TEM imaging, the *x* and *y* coordinates of the bacterial features of interest were recorded with a TEM stage readout. The cryo-holder was then removed from the TEM and transferred to the dry pumping station (DPS) (Gatan). The holder with the sample was gradually brought to room temperature (RT) using the warm-up cycle and reinserted into the transmission electron microscope, and images of the specimen were collected while at RT. Although the marked positions did not align exactly with the material due to the general contraction of the sublimated material, it was easy to identify the previously imaged areas. The main advantage of this methodology was to eliminate rotational shift. To simplify the alignment of the images obtained under the two conditions, series of images were collected at fixed magnifications. The images were aligned by using the "Layers" feature in Adobe Photoshop, and cell shrinkage in two dimensions (2D) was calculated by weighted correlation of 30 pairs of identical cells under both hydration conditions.

Cryo-SEM and cryo-FIB. For *S. oneidensis* MR-1 cell suspensions, a 5-μl drop was applied to a 200-mesh copper TEM grid with carbon-coated Formvar support film (EMS) adhered by double-sided adhesive carbon tape to an aluminum stub on the cold stage holder. After 1 min, the excess liquid was removed by wicking, and the sample was immediately plunged into the liquid nitrogen with a device within the Quorum PPT2000 cryo-preparation stage (Polaron, Quorum Technologies, United Kingdom). After the vacuum was applied to create a semi-slush consistency of liquid nitrogen, the holder with the sample was raised and cryo-transferred at the temperature of liquid nitrogen vapors to the cryo-preparation chamber. To emphasize the three-dimensional (3D) cellular structures, the upper layer of amorphous water was briefly sublimated at −95°C before the temperature was lowered to −160°C. The sample was coated with Pt and transferred to the cooled stage of the Helios 600 Nanolab dual-beam scanning electron microscope (FEI) for imaging.

For biofilms, a small piece of fully hydrated natural biofilm was transferred onto the cryo-scanning EM (cryo-SEM) cryo-specimen holder coated with carbon tape and allowed to adhere for 1 min. The residual liquid was removed with the tip of filter paper and immediately plunged into the liquid nitrogen as described above. The biofilm sample was sputter -coated with a few nanometers of Pt in the cryo-preparation chamber and transferred to the cooled stage of a Helios microscope. The samples were initially imaged at −180°C by secondary electron detectors; to emphasize the 3D structure of the biofilm, the temperature was briefly raised (−160°C for 2 min) to sublimate out ("freeze-etch") the upper layer of amorphous water, including nanocrystalline ice on the very surface. Furthermore, by using the heating stage, the temperature was increased with 20°C increments (in 10 continual steps from −160 to +20°C, allowing 20 min between each temperature change). This way, the dynamic biofilm structural changes could be observed during the dehydration. The images and real-time movies were acquired at each time point for structural comparison of the cellular material (see Movie S1 in the supplemental material). For the cryo-focused ion beam (cryo-FIB) of the selected biofilm regions, the stage was tilted to 52°, and a protective platinum layer was applied before FIB milling. Thirty kilovolts and a beam current in the range from 1 to 10 nA (10 nA for rough milling and 1 nA for cleanup cut) in an area 40 μm wide and approximately 15 μm deep were used to progressively cut and remove the material in the direction perpendicular to the biofilm surface.

TEM preparation by HPF and AFS. High-pressure freezing (HPF) and automatic freeze substitution (AFS), followed by plastic embedding, were used to produce thin sections of (i) *S. oneidensis* MR-1 cell suspensions and (ii) natural biofilms. (i) For thin sectioning of cell suspensions, the cells were pelleted by brief centrifugation with a quick-spin minicentrifuge and mixed with 0.5% agarose (Cambrex Bio Science Rockland, Inc., Rockland, ME), and then 3 μl of the suspension was transferred into an HPF flat specimen carrier and frozen with a Leica EM PACT high-pressure freezer (Leica Microsystems Inc., Bannockburn, IL) at a typical rate of 1,700°C/s. The pods with compacted frozen cells were transferred under liquid nitrogen to the precooled AFS (EM AFS; Leica), and a protocol for cell fixation, water substitution by acetone, and a gradual warm-up to RT was followed (see Table S1 in the supplemental material). After 72 h, the samples were released from the pods by a gentle liquid flow induction in the surrounding acetone. The samples were washed three times in acetone, gradually infiltrated with an ascending series of Spurr's low-viscosity embedding media (EMS) (25%, 50%, 75%, and three 100% washes for 120 min each), and cured at 60°C for 24 h. The polymerized blocks were sectioned to 70-nm thin sections with a Leica Ultracut UCT ultramicrotome, mounted on Formvar-coated 100 mesh Cu TEM grids sputtered with carbon, and poststained for 7 min with aqueous 2% uranyl acetate followed by 3 min of Reynolds' lead citrate (51) prior to TEM imaging. (ii) For thin sectioning of biofilms, the biofilms were infiltrated with 10% dextran for 15 min and prepared for HPF relative to their overall morphology. For thick biofilms, a flat piece was dissected using a sample punch (Leica no. 706892), and the material was frozen in a specimen carrier by using Leica EM PACT. For biofilms with a more dispersed nonoriented structure, the material was manipulated into the copper specimen tubes of HPF pods by using a cellulose microcapillary (Leica no. 706869) inserted into a Cu microtube to help the capillary action to drawing the biofilm into the tube. After the HPF, both types of biofilm samples were transferred under liquid nitrogen to the AFS unit and processed for plastic embedding as described above. No poststaining was applied due to the sufficient contrast provided by the soluble mineral portion.

SEM preparation. One milliliter of planktonic *S. oneidensis* MR-1 cells or a selected portion of bacterial biofilm was applied to the 0.2-μm-pore polycarbonate track-etched membrane filters placed on top of filter paper in a petri dish, and cells were allowed to adhere for 1 min. Excess liquid was removed by micropuncturing the filter membrane with fine-tip forceps. The wet membranes were folded and transferred into vials where all subsequent washes were carried out to prevent cell loss during the numerous fluid exchanges. The samples were processed in one of three ways: (i) aldehyde fixation and ethanol dehydration followed by critical point drying (CPD) (method a); (ii) ruthenium red-lysine fixation, dehydration, and CPD (method b); and (iii) air-drying (method c). For method a, the membranes with cells or biofilms were fixed in 2.5% glutaraldehyde (EMS) for 1 h, washed three times in phosphate-buffered saline (PBS), and gradually dehydrated in an ethanol series (25%, 33%, 50%, 75%, and 90% and three times at 100%, 15 min each). After dehydration, the membranes with cells were placed into the precooled processing chamber of a CPD instrument (Pelco CPD2; Ted Pella, Inc., Redding, CA) and processed according to an automated CPD scheme, reaching a temperature of 35°C at 1,200 lb/in^2, with CO_2 as a transitional fluid. The CPD-processed membranes were mounted on standard aluminum SEM stubs covered with double-sided carbon adhesive tape and sputter-coated with carbon. For method b, to stabilize the delicate EPS structures, a slightly modified ruthenium red-lysine fixation protocol (15) was followed. Briefly, the samples were incubated with a stain cocktail containing 0.075% ruthenium red (Sigma, St. Louis, MO), 30 mM lysine (Sigma), 2% paraformaldehyde (EMS), and 2.5% glutaraldehyde in 0.1 M sodium cacodylate buffer (EMS). After 30 min, the membranes were washed three times in 0.1 M cacodylate buffer and dehydrated in ethanol series, and CPD was performed as described above. For method c, the air drying was carried out without ethanol dehydration or CPD in selected samples to evaluate the effects of transitional solvents on cell shrinkage. Samples were sputter coated with carbon upon complete dehydration by air drying. All samples were evaluated at RT in the scanning electron microscope at 2 kV.

Microscopy. TEM samples were examined with the Tecnai T-12 transmission electron microscope (FEI) operating at 120 kV with an LaB_6 filament, equipped with a high-tilt stage for tomography and a cryostage. Images were collected digitally with a 2x2K Ultrascan 1000 charge-coupled device with a "U" scintillator (Gatan) calibrated to the transmission electron microscope camera length to enable direct measurements correlated with the magnification of the acquired images. DigitalMicrograph (Gatan) software was used for imaging and analyses of cellular features. Cryo-SEM imaging was performed at a Helios 600 Nanolab dual-beam microscope (FEI) coupled with a Quorum PPT2000 cryo-preparation stage (Polaron, Quorum Technologies, United Kingdom). The room temperature high-resolution imaging and the electron energy loss spectroscopy (EELS) analysis (see the supplemental material) were performed on a JEOL2010 transmission electron microscope (JEOL, Ltd., Japan) equipped with a Gatan image filter GIF2000 (Gatan) and Gatan 1x1K charge-coupled device (CCD). Absorption edges determined by EELS were analyzed by comparison of unknowns to standards of known oxidation state (19). For room temperature SEM, samples were evaluated in a LEO 982 field emission scanning electron microscope (Zeiss, Thornwood, NY).

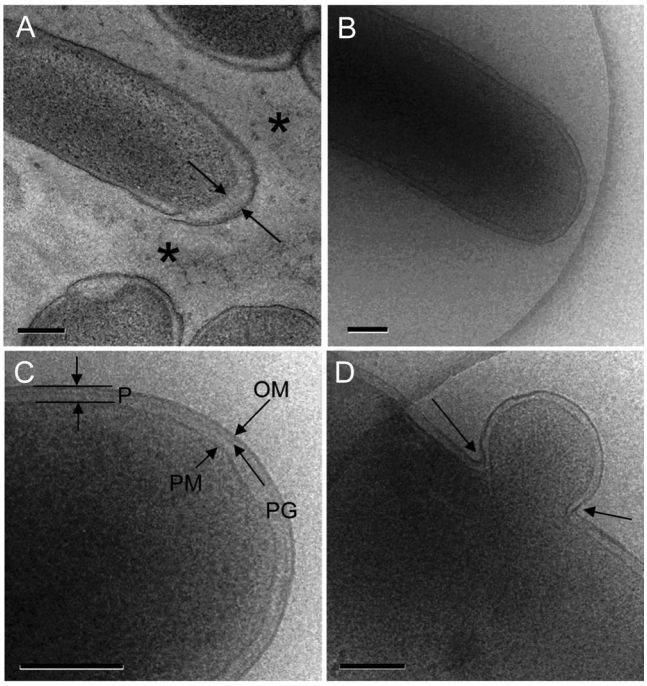

FIG. 1. Comparison of fine-scale bacterial cell features as revealed by HPF/AFS processing and cryo-TEM. The morphology of *S. oneidensis* MR-1 cells processed by HPF followed by AFS (A) showed the most accurate cell features of all traditional chemical fixation sample preparation methods, including intact periplasm, with some separation in the membrane area (arrows). EPS appears condensed into random structures that are difficult to interpret in a cross-section (asterisks). (B) Bacteria imaged by cryo-TEM display exceptionally well-pronounced membranes; however, the EPS has a very low contrast, due to the high water content and generally the relatively dispersed nature of light elements. (C) Distinct features, such as outer and plasma membranes (OM and PM, respectively), defining the periplasm (P) and the peptidoglycan layer (PG) provide accurate morphological information that can be used for obtaining precise dimensions. Cryo-TEM also provides improved ultrastructural detail in bacterial processes: e.g., a membrane vesicle pinching off a cell (D). Resting-cell suspensions of *S. oneidensis* MR-1 were incubated anaerobically with lactate and fumarate, and representative assay aliquots were prepared for concurrent EM imaging. Scale bars: 200 nm (A, B, and D) and 500 nm (C).

RESULTS

Cryo-TEM. Cryo-TEM was used to acquire accurate ultrastructural image data on bacterial cells and associated EPS in their hydrated state. Bacterial suspensions prepared under controlled conditions were vitrified and imaged by cryo-TEM at −178°C by using the low-radiation-dose scheme (Fig. 1). The EPS produced by *S. oneidensis* MR-1 had a very low contrast due to the lack of electron density in this highly hydrated state and the absence of contrasting agents (Fig. 1B). The resulting cryo-TEM images of the whole cells were used to

obtain accurate measurements of cellular features such as the region between the outer surface of the plasma membrane (PM) and the inner face of the outer membrane (OM): i.e., the periplasm (24) (Fig. 1C). The dimensions of this region as determined by measurements from approximately 200 cells from each treatment were evaluated, and the mean width of the periplasm was determined to be 23.5 ± 3.7 nm. This is approximately 25% thicker than values previously obtained by more traditional methods involving thin sectioning of plastic-embedded cells processed by high-pressure freezing and freeze substitution (Fig. 1A). Although measurements of the width of the periplasm in Gram-negative bacteria vary (57), the typical width in *Escherichia coli* cells is 12 to 15 nm (35). Since the frozen-hydrated bacteria are as close to the natural state as currently obtainable, these periplasmic distances are plausibly among the most accurate ones. In contrast with more traditional TEM preparations, other hydrated cellular features (e.g., the peptidoglycan layer [Fig. 1C] and ribosomes [not shown]), were also identifiable. Vitrification also improved the visualization and spatial information of other cellular features such as blebbing of membrane vesicles (Fig. 1D).

Cryo-EM of hydrated EPS and associated mineral phases. Resting-cell suspensions of the dissimilatory metal-reducing bacterium *S. oneidensis* MR-1 were exposed to two metals in their most oxidized forms: (i) manganese [Mn(IV)] and (ii) uranium [U(VI)], respectively. These metals exhibit contrasting biogeochemical behaviors as a function of oxidation state: nanocrystalline MnO_2, a poorly soluble solid under the given incubation conditions, is reduced under anaerobic conditions by *S. oneidensis* MR-1 to Mn(II), which is relatively soluble (44, 45, 56). U(VI) is considerably more soluble, especially in the presence of complexing ligands such as carbonate relative to nanocrystalline UO_2 (uraninite), the primary product of U(VI) reduction (21, 33). The reaction kinetics for U(VI) and Mn(IV) reduction were characterized in our previous experiments, and the corresponding bacterial and mineral associations in the dehydrated state were imaged (18, 36). The high-resolution images of bacterial cells and EPS in their hydrated state specifically associated with nanoparticulate Mn oxide and the reduction end product [i.e., Mn(II) ions] were captured (Fig. 2). Cryo-TEM of cells incubated with nanocrystalline MnO_2 revealed that both the solid-phase Mn and soluble Mn are localized specifically within the EPS (Fig. 2A). The cryo-SEM provided additional support for our cryo-TEM observations as both cells and MnO_2 crystals were observed to be enrobed in an EPS matrix which became web-like and tapered into filaments upon cryo-SEM sample preparation (Fig. 2C). In contrast, RT TEM and SEM revealed that EPS shrank around MnO_2 crystals (Fig. 2B and D) and that collapsed EPS was untapered and appeared to interconnect many cells after CPD preparation for RT SEM (Fig. 2D). For Mn species identification, the cryo-TEM was coupled with the electron energy loss spectrometry (EELS) and high-resolution TEM imaging in the RT mode (see Fig. S1 in the supplemental material). The EELS showed mixed valence of Mn(II/III) associated with EPS produced by *S. oneidensis* MR-1. The unprecedented views of specific associations of EPS with Mn(II) and Mn(III) ions further substantiate our knowledge of a significant role for EPS in microbial mineral and metal interactions.

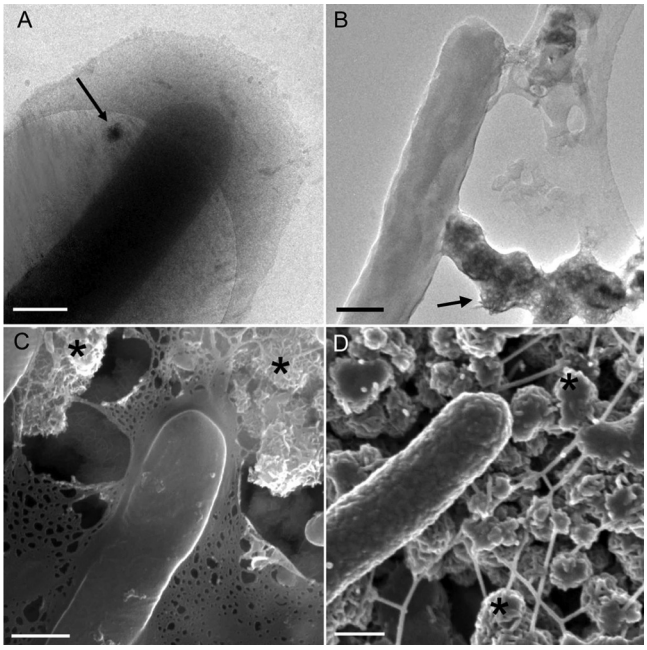

FIG. 2. Comparison of bacteria and EPS in the hydrated and dehydrated states. Resting-cell suspensions of *S. oneidensis* MR-1 were incubated anaerobically for 24 h with lactate and MnO_2, and representative assay aliquots were prepared for concurrent cryo-EM and RT EM imaging. (A) Cryo-TEM micrograph of cell illustrating EPS in the hydrated state. The slight contrast of the EPS is likely due to bound Mn(II) resulting from dissimilatory reduction of Mn(IV). The arrow in panel A shows the MnO_2 crystalline material. (B) The whole-mount RT TEM preparation shows a cell with the collapsed EPS covering the MnO_2 material (arrow). (C) Representative cryo-SEM image of rapidly frozen material after partial sublimation displays partially hydrated cells associated with EPS that covers the MnO_2 material (asterisks). (D) A fixed, dehydrated, and CPD-prepared sample characteristically shows excellent 3D cellular preservation but completely altered EPS that forms fiber-like structures colocalized with MnO_2 material (asterisks). Scale bars: 500 nm.

Changes in EPS morphology resulting from dehydration *in vacuo*. To demonstrate the susceptibility of EPS to dehydration-mediated structural collapse, the fully hydrated EPS was subjected to relatively slow dehydration by sublimation induced *in situ* under vacuum inside the TEM column, assisted by a slight temperature increase. These images captured how the originally highly hydrated, gel-like EPS undergoes dramatic physical changes (Fig. 3A to C). Upon exposure to a slow (~400-s), controlled temperature rise from the initial −178°C to −155°C, the phase transformation from the amorphous ice started, including nanocrystalline ice nucleation, followed by the partial release of unbound water under vacuum as sublimation proceeded. The EPS revealed surprising pliability as it began to collapse and condense into fiber-like structures that increasingly stretched between the areas where the material was anchored to the grid support. This phenomenon is in a good accordance with documented behavior of viscoelastic material under stress conditions that induce plastic deformation (11).

Cryo-TEM correlated with room temperature TEM. To compare the cell architectures in both the hydrated and dehydrated states, frozen-hydrated samples of *S. oneidensis* MR-1

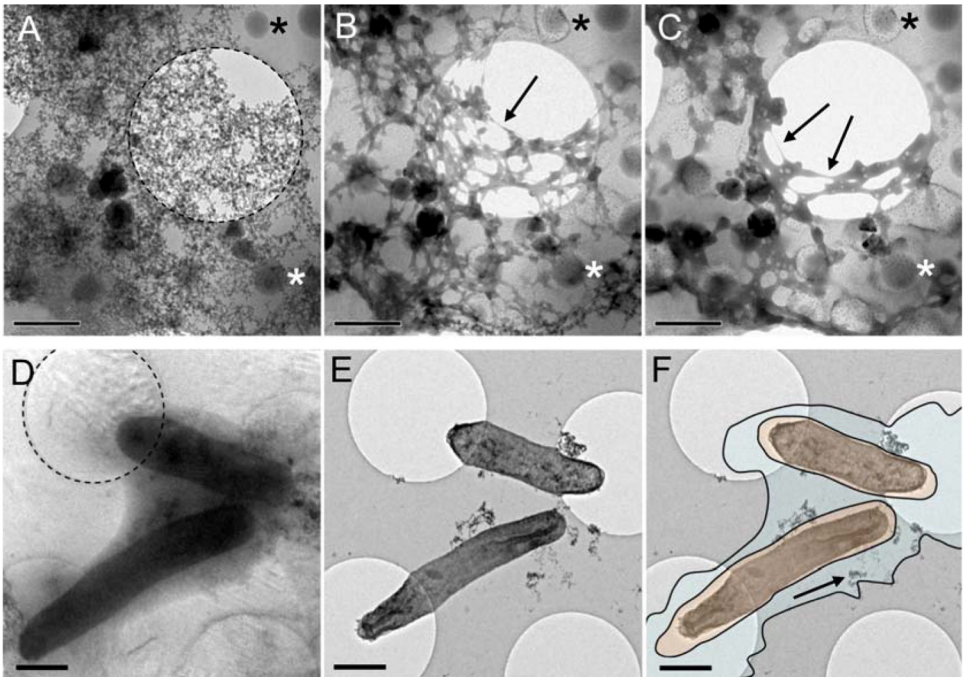

FIG. 3. (A to C) Progressive transformation of *S. oneidensis* MR-1 EPS during dehydration in the cryo-TEM. (A) Partly hydrated EPS of washed resting cells incubated with lactate and fumarate and without potential contrasting metal ions, supported by a carbon film. (The dashed circle outlines a hole in the support film.) (B and C) An assortment of secondary formed nanocrystalline ice particles covers the EPS surface. Large hexagonal ice crystals (asterisks) can serve as fiducial markers during the dynamic progression of the EPS dehydration. Arrows point to the newly formed EPS structures that form during transformation of the viscoelastic EPS that collapses due to the water loss during sublimation and nonelastic stretching between the points anchored to the carbon film. The time sequence from panels A to C was 200 s, with the electron beam blocked between the three low-dose exposures at a temperature of −152°C. (D to F) Comparison of cells and associated EPS surface area in the hydrated state and after subsequent dehydration. (D) Cryo-TEM image (−178°C) of cells incubated for 24 h with U(VI) and lactate. The visualization of EPS is enhanced by the contrast from soluble U(VI), and nascent UO_2 nanoparticles are observed within hydrated EPS. (E) Identical area after DPS sublimation to RT. (F) Superimposed cryo-TEM image with the outlines of the same two cells over the RT image illustrating substantial shrinkage and detachment of the EPS with the UO_2 precipitates distal to the cell surface (arrow). The estimated cellular linear volume loss was 29 to 41%. Scale bars in panels A to F represent 1 μm.

resting cells reducing uranyl U(VI) to nanoparticulate uraninite [$U(IV)O_2$] were first observed by cryo-TEM (Fig. 3D) and subsequently brought to RT in a DPS to facilitate correlated imaging in dehydrated state. After reaching RT, the identical regions of the dehydrated sample that were previously imaged in the frozen-hydrated state were reimaged (Fig. 3E). The corresponding cells had undergone considerable collapse and shrinkage relative to their dimensions in the hydrated, vitrified state. Dehydration resulted in a decrease in average cell area of ~29 to 41% relative to the average cell area in images from vitrified samples (calculated from 2D projections) (Fig. 3F). Moreover, the EPS underwent extensive condensation from the hydrated, gel-like state surrounding cells to a highly collapsed state which was difficult to identify after dehydration. Notably, the nascent UO_2 nanoparticles and U(VI) ions that were specifically bound by the predominantly negatively charged, hydrated EPS provided (i) extra support to the EPS matrix (nanocrystalline mineral phase) and (ii) additional contrast due to the higher electron density, essentially acting like a poststain.

Cryo-SEM and FIB examination of biofilms. In addition to the controlled laboratory studies of axenic *Shewanella* cultures, the morphology of mature, natural biofilms obtained from a uranium bioremediation field research site near Rifle, CO (1, 59), was also investigated. In the hydrated state at −180°C, the biofilm surface was covered by a smooth, thin layer of gel-like EPS enrobing bacteria (Fig. 4A and B). Upon sublimation to −150°C, cells became more pronounced within the EPS matrix, and the first signs of the EPS collapse could be observed, becoming more pronounced around −90°C (Fig. 4C and D). Analogous to the cryo-TEM observations of *S. oneidensis* MR-1 EPS, the dynamic structural changes of biofilms resulting from gradual dehydration in the cryo-SEM were documented by real-time imaging (see Movie S1 in the supplemental material). Sublimation induced distortion of biofilm surface features as extensive cracks formed in the initially cohesive material over time (Fig. 5A and B). The EPS structural integrity loss became exacerbated by the overall material shrinkage, creating an increased strain on the viscoelastic matrix. As the mechanical stress during sublimation progressed or after CPD preparation of samples, matrix collapse was observed, first in the form of branched, web-like strands, followed by the formation of rope-like filamentous structures often greater than 10 μm in length (Fig. 5A to D). The layer beneath the biofilm surface was imaged by creating a cross-section by *in situ* FIB milling of biofilm maintained under cryo or RT conditions. The cryo-FIB-generated cross-section revealed bacteria with

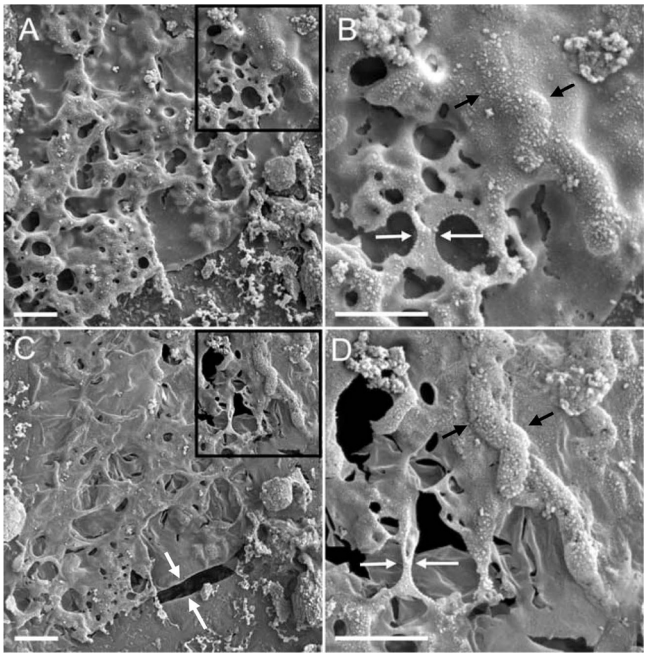

FIG. 4. Process of gradual moisture loss from frozen-hydrated natural biofilm as captured by cryo-SEM. (A and B) Initial image obtained at −180°C in the fully hydrated state after the biofilm was plunge-frozen. The black arrow in panel B points to a contour of bacteria embedded in EPS material that remains partially hydrated. (C and D) The same area of biofilm after sequential warming to −150°C. Notice the substantial collapse in the *z* direction (thickness), and beginning of the shrinkage in the *x* and *y* dimensions, resulting in cracks (white arrows in panel C). White arrows in panels B and D highlight the structural alteration of EPS, with the formation of a filamentous structure. The cellular features in panel D (black arrows) are more pronounced after sublimating a thin layer of the water from the surface. Black boxes in panels A and C illustrate the areas shown in higher magnification in panels B and D, respectively. Scale bars: 10 μm in panels A and C and 2 μm in panels B and D.

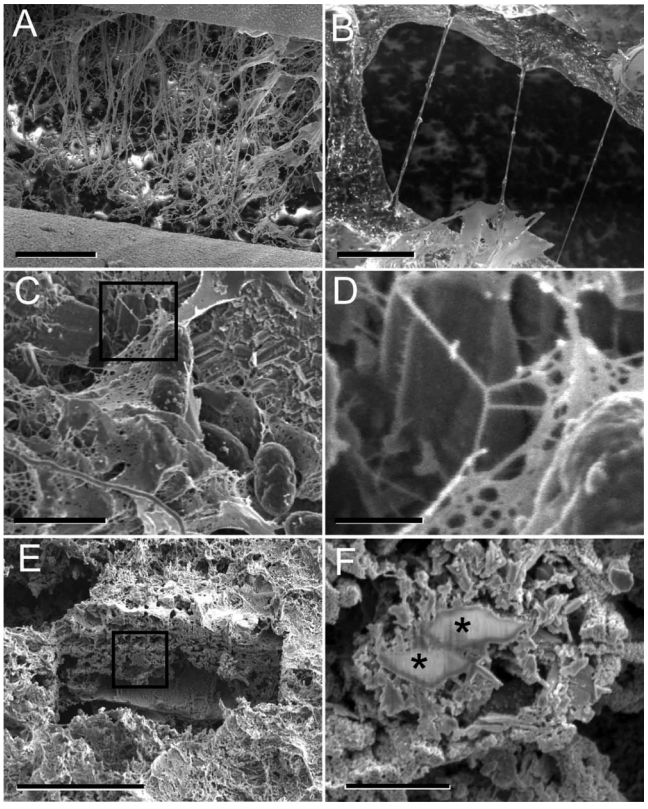

FIG. 5. Observation of biofilm features by cryo-SEM and RT SEM. (A and B) EPS transformation during sublimation induced by progressive warming in the cryo-SEM. The biofilm shows substantial structural damage due to material collapse and contraction induced by warming to −60°C. (A) Distortion of biofilm surface features with extensive cracks (>200 μm) developed over time in the initially cohesive material. (B) Formation of filamentous structures could be observed *in situ* during the surrounding material shrinkage, while the partially hydrated viscoeleastic EPS material was stretched between apparent anchored points. (C and D) Morphologically similar filamentous structures formed during sublimation were also observed in samples prepared by CPD and viewed at RT in the SEM. (E) Cryo-FIB milling of an approximately 20-μm depth below the biofilm surface revealed superior structure preservation. (F) Cryo-FIB-prepared area with mineral-laden layers of EPS and cells in various degrees of mineralization (asterisks), with no signs of EPS collapse and stretching. Black boxes in panels C and E illustrate the areas shown in higher magnification in panels D and F, respectively. Scale bars: 200 μm (A), 5 μm (B), 2 μm (C), 500 nm (D), 30 μm (E), and 2 μm (F).

different degrees of associated mineralization, as well as secondary mineral phases devoid of bacteria (Fig. 5E and F).

Images of EPS and bacteria in biofilms prepared by additional EM processing methods are included in the supplemental material for comparative purposes (see Fig. S2 and S3).

DISCUSSION

The highly hydrated associations of bacteria and EPS interacting with minerals and metals were systematically investigated with an array of cryo-EM and traditional EM techniques. The resulting conceptual model and respective correlated images illustrating the EPS structural changes induced by various EM sample-processing methods are presented in Fig. 6. Clearly, cryo-TEM is a superior method for maintaining the cells and EPS in their highly hydrated state, with excellent ultrastructural preservation (Fig. 6A and B). This methodology also produced extremely accurate measurements of the region exterior to the plasma membrane, the location of the catalytic electron transfer proteins in *S. oneidensis* MR-1 essential for metal and radionuclide reduction (3, 42). The amorphous structure of the EPS was observed; however, due to the high water content and light element composition, EPS has a very low electron density, resulting in low contrast (Fig. 1B). The visualization of this material by cryo-TEM was enhanced when soluble electron-dense metals [U(VI) or Mn(II)/(III)] were present (Fig. 2 and 3). RT TEM of frozen-hydrated cell suspensions subsequently sublimated in a weak vacuum of the DPS resulted in EPS dehydration and collapse into mesh-like structures that maintained the overall "footprint" of the hydrated EPS (Fig. 6C and D). Interestingly, the samples prepared by DPS sublimation also demonstrated improved spatial preservation of overall 3D structure even after progression to full dehydration. This was in contrast to the complete *z* direction collapse of cellular and EPS material observed with air-dried samples (TEM whole mounts) (Fig. 6E and F). When negatively stained with an electron-dense solution, bacterial

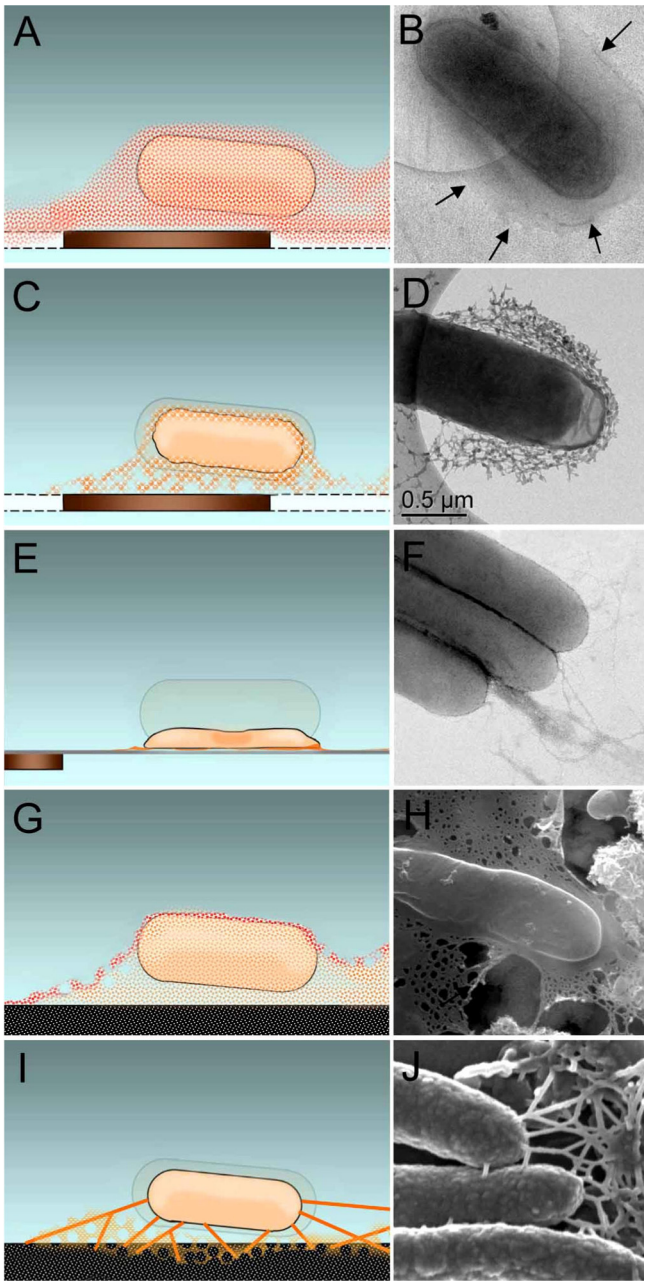

FIG. 6. Model and correlated EM images of cells and associated EPS structural alteration resulting from different methods of sample processing. (A and B) Cryo-TEM of frozen-hydrated cells vitrified in amorphous ice imaged at −178°C. Arrows indicate the outline of the EPS. (C and D) RT TEM of initially vitrified cells that have been gently dried in low vacuum of the DPS. (E and F) RT TEM of air-dried cells stained with Nano-W (Nanoprobes, Yaphank, NY) prior to imaging. (G and H) Cryo-SEM of cells in a thin layer of partially sublimated amorphous ice. (I and J) RT SEM of cells that were fixed, dehydrated, and prepared by CPD. Panels C, E, and I also show hydrated cell outline for comparison of cell shrinkage.

appendages such as flagella and pili can be imaged in great detail by this technique (Fig. 6F). Cryo-SEM maintained cells and EPS in a highly hydrated state, with the exception of a thin surface water layer that was intentionally sublimated to mitigate the buildup of water ice (Fig. 6G and H). If the temperature was further increased, thinning of the EPS due to the water loss became more prominent, and signs of dehydration such as the loss of the EPS integrity started to appear. The deformation of viscoelastic EPS material that was observed during sublimation resulted in the creation of features resembling the filamentous structures commonly present in dehydrated preparations (see Movie S1 in the supplemental material). In sample preparation by CPD, the solvents such as ethanol or acetone used as a transitional fluid for replacing cellular water can initially extract lipids and protein complexes, resulting in changes in cellular dimensions (shrinkage) (Fig. 6I and J). During the CPD process, after the substitution of transitional fluid with liquid CO_2, the material is exposed to simultaneous stresses of a strong laminar flow in the closed microfluidics environment, to a very high pressure and increased temperature inducing the phase transformation, and finally to complete dehydration. The exceptional preservation of turgid cells is a signature of this method; however we speculate that loosely supported EPS undergoes notable transformation, resulting in the distinctive filamentous connections between the cells and minerals. The structures would be predicted, based on the behavior of viscoelastic material, to have a narrowing region at the base of their attachment. However, these filaments, without the pronounced tapering region, are observed specifically in the CPD preparations. We believe these are secondary products of chemical processing and viscoelastic deformation of the EPS induced by this method.

There are two unsettled questions regarding bacterial EPS structure and function. The first question is what happens to this complex network of carbohydrate macromolecules, proteins, and lipids that entraps organic matter and contains up to 95% water and, in many cases, binds metal ions, when water is removed? The EPS can be expected to display rheological behavior of complex fluid under these conditions (32). During the dehydration process, functional groups are deprived of their —OH group, and as molecules of water are removed, condensation reactions on the EPS components occur. The originally flexible polysaccharides become rigid as they lose their glycosidic bonds that provide them with conformational flexibility. Proteins, partially denatured in the fixation step by aldehydes that cause cross-linking, are dehydrated by organic solvents such as ethanol or acetone, further inducing communal aggregation (6). In addition, organic solvents partially remove lipids, contributing to microstructure breakdown. It is also likely that shear conditions during the sample preparation may induce assembly of structures in a more dense form around linear polysaccharides ("backbone"), becoming increasingly rigid as the dehydration progresses. Together, these conditions promote the solution-gel phase transition of EPS to a network of interconnected fibrils and densification. Finally, upon further water removal, the viscosity of this supramolecular hydrogel increases, and eventually transformation to a solid state occurs.

The second question is what happens to ions in EPS upon dehydration? During the exposure to cationic metals, either naturally in solution or resulting from microbial biotransformation, hydrated EPS will bind the ions, concentrating them within the matrix (5). When EPS loses hydroxyl groups during dehydration, the increasing concentration of the ions within

the contracting polymer chains in the confined space will effectively increase the ionic strength that can result in the precipitation of salts, with implications for creating microenvironments with different physical and chemical properties.

Bacterial EPS can influence important geochemical processes, including oxidation/reduction, dissolution/precipitation, colloid transport, subsurface water flow, and contaminant movement *in situ* (17). Although the exact role(s) of EPS produced by *S. oneidensis* MR-1 during metal reduction remains undetermined, its production upon exposure to soluble or solid electron acceptors and the extracellular occurrence of reduced metals suggest that EPS could be an important component of this organism's extended electron transport system. Some metal-reducing *Shewanella* strains have been reported to secrete flavin-based electron shuttles (38, 58), produce EPS that contains outer membrane *c*-type cytochromes (36, 49), and evolve electron-conducting nanowires (22) under conditions of electron acceptor limitation, indicating that this organism may use multiple mechanisms for extracellular electron transfer. Whether hydrated EPS has a direct role in extracellular electron transfer or an indirect one, such as providing a supporting matrix for redox proteins, low-molecular-weight electron shuttles, or nanowires, remains to be determined.

Filamentous EPS structures observed in bacterial samples prepared and imaged by traditional EM methods have been suggested to be involved, directly or indirectly, in physical interactions and aggregation (27, 48), cell-to-surface attachment by tethering via thin adhesion threads (29), extracellular electron transfer (22), and possibly *de facto* electrical signaling within the structurally integrated communities (8). Although these are intriguing observations, our analysis illustrates how dehydration can severely alter chemical and physical properties of bacterial EPS that in turn can influence mechanistic interpretations of microbial processes. It is critical that the potential for generation of dehydration-induced changes on EPS structure and function is recognized and, when possible, avoided or minimized through the use of advanced cryo-EM methodologies that will enable further advances in understanding bacterial interactions with their environment.

ACKNOWLEDGMENTS

This research was performed at the Environmental Molecular Sciences laboratory (EMSL), a national scientific user facility sponsored by the U.S. DOE's Office of Biological and Environmental Research (OBER) and located at the Pacific Northwest National Laboratory (PNNL). Financial support was provided through an EMSL Research and Capability Development Proposal and the Subsurface Biogeochemical Research program (SBR). PNNL is operated for the DOE by Battelle Memorial Institute under contract DE-AC06-76RLO 1830.

We thank David Kennedy for the supporting kinetic studies of metal reduction, Steve Pfeiffer (Gatan, Inc.) for helpful discussions, and Libor Kovarik for the EELS data evaluation.

We dedicate this article to our colleague and mentor, world-renowned geomicrobiologist Terry J. Beveridge (1945 to 2007), whom we regard as the true pioneer in the high-resolution characterization of structural microbiology, with remarkable contributions in areas such as bacterial cell wall reactivity and microbial effects on metal speciation.

REFERENCES

1. **Anderson, R. T., et al.** 2003. Stimulating the *in situ* activity of *Geobacter* species to remove uranium from the groundwater of a uranium-contaminated aquifer. Appl. Environ. Microbiol. **69:**5884–5891.
2. **Bayer, M. E., and H. Thurow.** 1977. Polysaccharide capsule of *Escherichia coli*—microscope study of its size, structure, and sites of synthesis. J. Bacteriol. **130:**911–936.
3. **Beliaev, A. S., D. A. Saffarini, J. L. McLaughlin, and D. Hunnicutt.** 2001. MtrC, an outer membrane decahaem *c* cytochrome required for metal reduction in *Shewanella putrefaciens* MR-1. Mol. Microbiol. **39:**722–730.
4. **Beveridge, T. J.** 2005. Bacterial cell wall structure and implications for interactions with metal ions and minerals. J. Nucl. Radiochem. Sci. **6:**7–10.
5. **Beveridge, T. J., and R. J. Doyle.** 1989. Metal ions and bacteria. Wiley and Sons, Inc., New York, NY.
6. **Bozzola, J. J., and L. D. Russell.** 1999. Electron microscopy: principles and techniques for biologists. Jones and Bartlett, Sudbury, MA.
7. **Briegel, A., et al.** 2006. Multiple large filament bundles observed in *Caulobacter crescentus* by electron cryotomography. Mol. Microbiol. **62:**5–14.
8. **Costerton, J. W.** 2007. The biofilm primer. Springer, Berlin, Germany.
9. **Decho, A. W.** 1990. Microbial exopolymer secretions in ocean environments: their role(s) in food webs and marine processes. Oceanogr. Mar. Biol. Annu. Rev. **28:**73–153.
10. **Decho, A. W., P. T. Visscher, and R. P. Reid.** 2005. Production and cycling of natural microbial exopolymers (EPS) within a marine stromatolite. Palaeogeogr. Palaeoclimatol. Palaeoecol. **219:**71–86.
11. **Dill, E. H.** 2006. Continuum mechanics: elasticity, plasticity, viscoelasticity, CRC Press, New York, NY.
12. **Erk, I., G. Nicolas, A. Caroff, and J. Lepault.** 1998. Electron microscopy of frozen biological objects: a study using cryosectioning and cryosubstitution. J. Microsc. (Oxf.) **189:**236–248.
13. **Erlandsen, S. L., C. J. Kristich, G. M. Dunny, and C. L. Wells.** 2004. High-resolution visualization of the microbial glycocalyx with low-voltage scanning electron microscopy: dependence on cationic dyes. J. Histochem. Cytochem. **52:**1427–1435.
14. **Fassel, T. A., and C. E. Edmiston.** 1999. Bacterial biofilms: strategies for preparing glycocalyx for electron microscopy. Methods Enzymol. **310:**194–203.
15. **Fassel, T. A., and C. E. Edmiston (ed.).** 2000. Evaluating adherent bacteria and biofilm using electron microscopy. Humana Press, Totowa, NJ.
16. **Flemming, H. C., T. R. Neu, and D. J. Wozniak.** 2007. The EPS matrix: the house of biofilm cells. J. Bacteriol. **189:**7945–7947.
17. **Fredrickson, J. K., and M. Fletcher.** 2001. Subsurface microbiology and biogeochemistry. Wiley & Sons, New York, NY.
18. **Fredrickson, J. K., et al.** 2002. Influence of Mn oxides on the reduction of uranium(VI) by the metal-reducing bacterium *Shewanella putrefaciens*. Geochim. Cosmochim. Acta **66:**3247–3262.
19. **Garvie, L. A. J., and A. J. Craven.** 1994. High-resolution parallel electron-energy-loss spectroscopy of Mn L(2,3)-edges in inorganic manganese compounds. Phys. Chem. Miner. **21:**191–206.
20. **Glaeser, R. M.** 2008. Cryo-electron microscopy of biological nanostructures. Phys. Today **61:**48–54.
21. **Gorby, Y. A., and D. R. Lovley.** 1992. Enzymatic uranium precipitation. Environ. Sci. Technol. **26:**205–207.
22. **Gorby, Y. A., et al.** 2006. Electrically conductive bacterial nanowires produced by *Shewanella oneidensis* strain MR-1 and other microorganisms. Proc. Natl. Acad. Sci. U. S. A. **103:**11358–11363.
23. **Graham, L. L., and T. J. Beveridge.** 1990. Effect of chemical fixatives on accurate preservation of *Escherichia coli* and *Bacillus subtilis* structure in cells prepared by freeze-substitution. J. Bacteriol. **172:**2150–2159.
24. **Graham, L. L., T. J. Beveridge, and N. Nanninga.** 1991. Periplasmic space and the concept of the periplasm. Trends Biochem. Sci. **16:**328–329.
25. **Graham, L. L., R. Harris, W. Villiger, and T. J. Beveridge.** 1991. Freeze-substitution of Gram-negative eubacteria. General cell morphology and envelope profiles. J. Bacteriol. **173:**1623–1633.
26. **Hunter, R. C., and T. J. Beveridge.** 2005. High-resolution visualization of Pseudomonas aeruginosa PAO1 biofilms by freeze-substitution transmission electron microscopy. J. Bacteriol. **187:**7619–7630.
27. **Ishii, S., T. Kosaka, K. Hori, Y. Hotta, and K. Watanabe.** 2005. Coaggregation facilitates interspecies hydrogen transfer between *Pelotomaculum thermopropionicum* and *Methanothermobacter thermautotrophicus*. Appl. Environ. Microbiol. **71:**7838–7845.
28. **Kachlany, S. C., et al.** 2001. Structure and carbohydrate analysis of the exopolysaccharide capsule of *Pseudomonas putida* G7. Environ. Microbiol. **3:**774–784.
29. **Kolari, M., U. Schmidt, E. Kuismanen, and M. S. Salkinoja-Salonen.** 2002. Firm but slippery attachment of *Deinococcus geothermalis*. J. Bacteriol. **184:**2473–2480.
30. **Korenevsky, A., and T. J. Beveridge.** 2007. The surface physicochemistry and adhesiveness of *Shewanella* are affected by their surface polysaccharides. Microbiology-SGM **153:**1872–1883.
31. **Kostka, J., and K. H. Nealson.** 1998. Isolation, cultivation and characterization of iron- and manganese-reducing bacteria, p. 58–78. *In* R. S. Burlage, R. Atlas, D. Stahl, G. Geesey, and G. Sayler (ed.), Techniques in microbial ecology. Oxford University Press, New York, NY.
32. **Larson, R. G.** 1999. The structure and rheology of complex fluids. Oxford University Press, New York, NY.
33. **Lovley, D. R., E. J. P. Phillips, Y. A. Gorby, and E. R. Landa.** 1991. Microbial reduction of uranium. Nature **350:**413–416.
34. **Lunsdorf, H., I. Kristen, and E. Barth.** 2006. Cationic hydrous thorium

dioxide colloids—a useful tool for staining negatively charged surface matrices of bacteria for use in energy-filtered transmission electron microscopy. BMC Microbiol. **6:**59.
35. **Madigan, M. T., J. M. Martinko, P. V. Dunlap, and D. P. Clark.** 2008. Brock biology of microorganisms, 12th ed. Benjamin Cummings, San Francisco, CA.
36. **Marshall, M. J., et al.** 2006. *c*-type cytochrome-dependent formation of U(IV) nanoparticles by *Shewanella oneidensis*. PLoS Biol. **4:**1324–1333.
37. **Marshall, M. J., et al.** 2008. Hydrogenase- and outer membrane *c*-type cytochrome-facilitated reduction of technetium(VII) by *Shewanella oneidensis* MR-1. Environ. Microbiol. **10:**125–136.
38. **Marsili, E., et al.** 2008. *Shewanella* secretes flavins that mediate extracellular electron transfer. Proc. Natl. Acad. Sci. U. S. A. **105:**3968–3973.
39. **McIntosh, J. R. (ed.).** 2007. Cellular electron microscopy, vol. 79. Elsevier, San Diego, CA.
40. **McLean, J. S., et al.** 2008. Oxygen-dependent autoaggregation in *Shewanella oneidensis* MR-1. Environ. Microbiol. **10:**1861–1876.
41. **Montesinos, E., I. Esteve, and R. Guerrero.** 1983. Comparison between direct methods for determination of microbial cell-volume: electron-microscopy and electronic particle sizing. Appl. Environ. Microbiol. **45:**1651–1658.
42. **Myers, J. M., and C. R. Myers.** 2001. Role for outer membrane cytochromes OmcA and OmcB of *Shewanella putrefaciens* MR-1 in reduction of manganese dioxide. Appl. Environ. Microbiol. **67:**260–269.
43. **Neal, A. L., et al.** 2007. Terminal electron acceptors influence the quantity and chemical composition of capsular exopolymers produced by anaerobically growing *Shewanella* spp. Biomacromolecules **8:**166–174.
44. **Nealson, K. H., R. R. Rosson, and C. R. Myers.** 1989. Mechanisms of oxidation and reduction of manganese. *In* T. J. Beveridge and R. J. Doyle (ed.), Metal ions and bacteria, Wiley and Sons, Inc., New York, NY.
45. **Nealson, K. H., and D. Saffarini.** 1994. Iron and manganese in anaerobic respiration—environmental significance, physiology, and regulation. Annu. Rev. Microbiol. **48:**311–343.
46. **Paerl, H. W., T. F. Steppe, and R. P. Reid.** 2001. Bacterially mediated precipitation in marine stromatolites. Environ. Microbiol. **3:**123–130.
47. **Palsdottir, H., et al.** 2009. Three-dimensional macromolecular organization of cryofixed *Myxococcus xanthus* biofilms as revealed by electron microscopic tomography. J. Bacteriol. **191:**2077–2082.
48. **Prigent-Combaret, C., et al.** 2000. Developmental pathway for biofilm formation in curli-producing *Escherichia coli* strains: role of flagella, curli and colanic acid. Environ. Microbiol. **2:**450–464.
49. **Reardon, C. L., et al.** 2010. Role of outer-membrane cytochromes MtrC and OmcA in the biomineralization of ferrihydrite by *Shewanella oneidensis* MR-1. Geobiology **8:**56–68.
50. **Reese, S., and B. Guggenheim.** 2007. A novel TEM contrasting technique for extracellular polysaccharides in in vitro biofilms. Microsc. Res. Tech. **70:**816–822.
51. **Reynolds, E. S.** 1963. Use of lead citrate as an electron-opaque stain in electron microscopy. J. Cell Biol. **17:**208.
52. **Schadler, S., C. Burkhardt, and A. Kappler.** 2008. Evaluation of electron microscopic sample preparation methods and imaging techniques for characterization of cell-mineral aggregates. Geomicrobiol. J. **25:**228–239.
53. **Schooling, S. R., and T. J. Beveridge.** 2006. Membrane vesicles: an overlooked component of the matrices of biofilms. J. Bacteriol. **188:**5945–5957.
54. **Seybert, A., R. Herrmann, and A. S. Frangakis.** 2006. Structural analysis of *Mycoplasma pneumoniae* by cryo-electron tomography. J. Struct. Biol. **156:**342–354.
55. **Stukalov, O., A. Korenevsky, T. J. Beveridge, and J. R. Dutcher.** 2008. Use of atomic force microscopy and transmission electron microscopy for correlative studies of bacterial capsules. Appl. Environ. Microbiol. **74:**5457–5465.
56. **Tebo, B. M., et al.** 2004. Biogenic manganese oxides: properties and mechanisms of formation. Annu. Rev. Earth Planet. Sci. **32:**287–328.
57. **Van Wielink, J. E., and J. A. Duine.** 1990. How big is the periplasmic space? Trends Biochem. Sci. **15:**136–137.
58. **von Canstein, H., J. Ogawa, S. Shimizu, and J. R. Lloyd.** 2008. Secretion of flavins by *Shewanella* species and their role in extracellular electron transfer. Appl. Environ. Microbiol. **74:**615–623.
59. **Vrionis, H. A., et al.** 2005. Microbiological and geochemical heterogeneity in an *in situ* uranium bioremediation field site. Appl. Environ. Microbiol. **71:**6308–6318.
60. **Webster, P., S. Wu, S. Webster, K. A. Rich, and K. McDonald.** 2004. Ultrastructural preservation of biofilms formed by non-typeable *Hemophilus influenzae*. Biofilms **1:**165–182.
61. **Wingender, J., T. R. Neu, and H.-C. Fleming.** 1999. What are bacterial extracellular polymeric substances?, p. 1–20. *In* J. Wingender, T. R. Neu, and H.-C. Fleming (ed.), Microbial extracellular polymeric substances. Springer, New York, NY.
62. **Zhang, P. J., C. M. Khursigara, L. M. Hartnell, and S. Subramaniam.** 2007. Direct visualization of *Escherichia coli* chemotaxis receptor arrays using cryo-electron microscopy. Proc. Natl. Acad. Sci. U. S. A. **104:**3777–3781.